Ultrasonics Sonochemistry 80 (2021) 105832

Contents lists available at ScienceDirect

Ultrasonics Sonochemistry

journal homepage: www.elsevier.com/locate/ultson

Ultrasound cavitation induced nucleation in metal solidification: An analytical model and validation by real-time experiments

Haijun Huang [a,b,c,1], Ling Qin [d,1], Haibin Tang [e,c,1], Da Shu [b,*], Wentao Yan [c,f,*], Baode Sun [b], Jiawei Mi [b,d,*]

[a] School of Materials and Chemistry, University of Shanghai for Science and Technology, Shanghai 200093, China
[b] Shanghai Key Lab of Advanced High-temperature Materials and Precision Forming, School of Materials Science and Engineering, Shanghai Jiao Tong University, Shanghai 200240, China
[c] Department of Mechanical Engineering, National University of Singapore, Singapore 117575, Singapore
[d] Department of Engineering, University of Hull, HU6 7RX, UK
[e] School of Intelligent Manufacturing, Nanjing University of Science & Technology, Nanjing 210094, China
[f] NUS Research Institute (NUSRI), Suzhou, Jiangsu 215123, China

ARTICLE INFO

Keywords:
Modelling
Ultrasound melt processing
Ultrasound Cavitation
Nucleation of metal alloys
Ultrafast synchrotron X-ray imaging and tomography

ABSTRACT

Microstructural refinement of metallic alloys via ultrasonic melt processing (USMP) is an environmentally friendly and promising method. However, so far there has been no report in open literature on how to predict the solidified microstructures and grain size based on the ultrasound processing parameters.In this paper, an analytical model is developed to calculate the cavitation enhanced undercooling and the USMP refined solidification microstructure and grain size for Al-Cu alloys. Ultrafast synchrotron X-ray imaging and tomography techniques were used to collect the real-time experimental data for validating the model and the calculated results. The comparison between modeling and experiments reveal that there exists an effective ultrasound input power intensity for maximizing the grain refinement effects for the Al-Cu alloys, which is in the range of 20-45 MW/m^2. In addition, a monotonous increase in temperature during USMP has negative effect on producing new nuclei, deteriorating the benefit of microstructure refinement due to the application of ultrasound.

1. Introduction

Most metals or metallic alloys are crystalline materials with polycrystal grain structures. Controlling the nucleation and growth of polycrystal grains through the solidification processes to achieve a desired microstructure and chemical homogeneity is the most commonly used technical approach in metal industry. Microstructure or grain refinement through solidification is often made via a chemical method by adding grain-inoculating elements into an alloy melt, acting as heterogeneous nucleation agents to increase the number and rate of nuclei. It can also be achieved via a physical method by applying external fields (e.g. electromagnetic fields or ultrasonic waves) into a solidifying melt to influence or control grain nucleation and subsequent grain growth. Chemical elements that are effective for grain-inoculating are alloy specific, i.e. different alloy systems need different type of chemical elements. For example, Ti and B for Al alloys [1], and Zr for Mg alloys [2], etc. The problems common to most grain-inoculating chemicals are (1) low inoculation efficiency, (2) added materials or operation cost, (3) undesired melt contamination and (4) negative environment impact. In recent years, as a part of the worldwide effort to reduce the Green House Gas Emission caused by industry activities, in the materials manufacturing and metallurgy sector, there has been a renewed worldwide interest and investment in developing green technologies with low energy consumption and low environment impact. In this aspect, the external physical field methods, in particular, the ultrasonic melt processing (USMP) technique, has attracted considerable interest in the materials research community and industry [3–6]. USMP has the combined benefits and capabilities to deliver efficient melt degassing and grain structure refinement in a single continuous operation

* Corresponding authors at: School of Materials Science and Engineering, Shanghai Jiao Tong University, Shanghai 200240, China (D. Shu); Department of Mechanical Engineering, National University of Singapore, Singapore 117575, Singapore (W. Yan); Department of Engineering, University of Hull, HU6 7RX, UK (J. Mi).
E-mail addresses: dshu@sjtu.edu.cn (D. Shu), mpeyanw@nus.edu.sg (W. Yan), J.Mi@hull.ac.uk (J. Mi).
[1] The author contributes equally

https://doi.org/10.1016/j.ultsonch.2021.105832
Received 20 October 2021; Received in revised form 10 November 2021; Accepted 13 November 2021
Available online 16 November 2021

Nomenclature

ΔH	enthalpy of phase change
ΔH_0	reference enthalpy of phase change, 10.7 kJ/mol at atmospheric pressure [44]
ΔV	molar volume difference between solid and liquid phases, assumed constant in this paper
ΔVa	volume for activation
β	cavitation bubble content
γ	gas polytrophic exponent
η	absolute viscosity of melt
η_0	a pre-potential viscosity factor
η_t	time-efficiency parameter
μ	melt viscosity
ρ	density of solid
ρ_0	reference density of solid at atmospheric pressure
σ	surface tension
σ_{sl0}	reference energy of solid–liquid interface, assumed 0.14 J/m^2 at atmospheric pressure [45]
σ_{sl}	solid–liquid interfacial energy
τ	life time of pressure pulse
a	time parameter
B	empirical constant
c	sound speed at atmospheric pressure
C_1	fitting constant
C_2	fitting constant
d_c	cavitation depth
D_{gs}	grain size
f	size-distribution of cavitation bubbles
f_u	ultrasound frequency, 20 kHz
h	Plank constant, 6.626×10^{-34} J·s
I_0	Iniital inputacoustic intensity
I_{th}	Pressure threshold for cavitation, assumed 1 MPa for pure melt [8]
j	constant, 1.4 for an adiabatic collapse [21]
k	Boltzmann constant, $1.3806488 \times 10^{-23}$ J/K
n	atom number per unit volume
N	Avogadro constant, 6.022141×10^{23}
n_i	number of identical cavitation bubbles marked by i
N_i	nucleus number induced by cavitation bubble i
N_I	total number in cavitation region
N_t	nucleus number induced by a multi-bubble system
p_{osc}	oscillation released pressure at bubble wall
Q_a	active energy
R_0	initial cavitation bubble radius
R_2	maximal bubble radius
R_d	down-limit of integration
R_i	minimal bubble radius
R_u	up-limit of integration
s	area of the ultrasound emitting surface, 3 mm^2
T	temperature, K
T_m	melting temperature of the alloy
T_{m0}	reference melting temperature
V	molar volume of the melt
V_c	cavitation region
V_{mol}	molar volume of solid phase
V_{pool}	melt volume

regardless of the alloy chemistry.

Previous research on USMP has identified three main mechanisms for ultrasound enhanced grain nucleation, namely, (1) cavitation induced homogenous nucleation, (2) cavitation activated heterogeneous nucleation, and (3) cavitation or acoustic flow-induced grain multiplication [7–9].

Cavitation induced homogeneous nucleation is due to the instantaneous pressure spike generated at ultrasonic bubble implosion. From thermodynamic point of view, such a sudden pressure spike increases the actual melting temperature of the melt in the vicinity of the imploding bubble. This effectively increases the level of undercooling for the melt nearby the imploded bubble, resulting in an increase in the driving force for homogeneous nucleation [10,11]. Cavitation activated heterogeneous nucleation is based on the hypothesis that the imploding or oscillating bubbles are able to activate or enhance the wetting capability of some non-metallic inclusions or second phases present in the melt. Consequently, such inclusions or second phases are "activated" as effective nucleation sites [12,13]. The grain multiplication mechanism is due to the fragmentation of intermetallic or dendritic phases under the shock wave emitted at bubble implosion or cyclic fatigue effect under the oscillation of ultrasonic bubbles [11]. In recent years, systematic in-situ synchrotron X-ray high-speed imaging studies [14,15] have provided unambiguous real-time evidence for the cavitation enhanced heterogeneous nucleation theory and grain multiplication theory in different alloy systems [16,17].

However, due to the spatial and temporal resolution limit for synchrotron X-ray imaging (currently the best combination reported in metal solidificaiton research is ~ 1 μm at 271,554 frame per second [16]), so far, directly observed evidence for cavitation-induced homogeneous nucleation, i.e. increasing in grain nucleation rate due to the implosion of ultrasonic bubbles have not been obtained, although limited and indirect observation has been reported recently [18]. Because of the technical constraint and inherent difficulty to make useful and sensible real-time and direct observation for such highly dynamic phenomena in metal solidification experiments, historically, analytical or modelling approaches have been used and adopted. Water-based solutions were often used as the model systems to obtain relevant evidence or data for model validation. For example, Inada et al. [19,20] proposed a water–ice transformation probability function and linked the number of bubble nuclei to the undercooling of water. They calculated the time lag between the instant of applying ultrasonic irradiation and the onset of ice nucleation. They also calculated the probability of ice nucleation for a given size-distribution of the initial bubbles [20]. Virone [21] proposed a simple analytical model that can be used to calculate the nucleation rate induced by ultrasonic cavitation. It can also calculate the number of nuclei as a function of the pressure of the collapsed bubbles in a supersaturated ammonium sulphate solution. They found that the nucleation rate increased with the pressure, and it was the dominant factor compared to the initial supersaturation. However, the model is not valid when the collapse pressure is over 7000 bar. Saclier [22] proposed another model to compute the number of nuclei in a water–ice system with multi-bubbles. It can calculate the pressure field in the vicinity of an imploding bubble, and the nucleation rate around the bubble. Cogne et al. [23,24] recently derived a refined model that is able to incorporate the melt temperature profile and then calculate the nucleation rate around a single bubble in water. They found that the melt temperature at an imploding bubble wall is much closer to the ambient temperature than the inner bubble, due to heat conduction from the bubble centre or the latent heat release. Such a phenomenon could affect the nucleation in the nearby volume.

So far, such analytical and modelling approaches have not been seen reported in metal alloy melts. The models developed from a water–ice system and other non-metallic transparent substances cannot be simply transferred to a metallic system. Metallic melts have different physical properties in the liquid state (e.g. atomic structure, viscosity, thermal conductivity, density), leading to different cavitation thresholds and

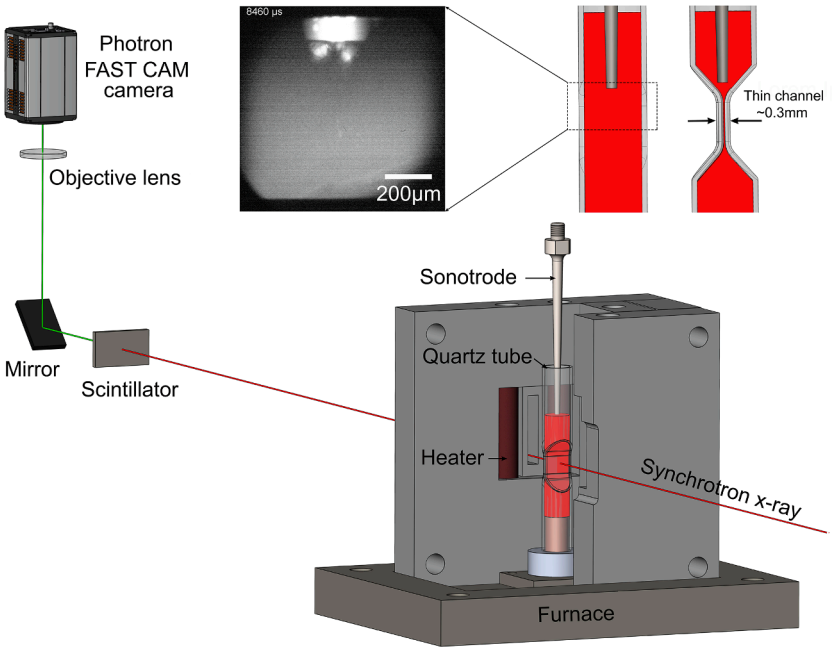

Fig. 1. The experimental set-up and sample arrangement for the real-time ultrafast synchrotron X-ray imaging experiments. A bespoke furnace with cartridge heaters (the front part was opened to show the specially-designed quartz sample holder and the sonotrode) was used for melting the alloy. The sample holder, sonotrode tip and alloy melt are enlarged and shown at the top right-hand side. The quartz tube sample holder has a thin channel of 0.3 mm thick in the middle for X-ray imaging (see the side sectional view and the front view of the quartz tube). Three K-type thermocouples were positioned at the top, middle and bottom of the thin channel to measure the temperatures of the melt.

bubble characteristics (i.e. size of cavitation zone, size of bubble, bubble number density and distribution). These factors affect the sononucleation events to a certain extent. More importantly, until now, there are lack of ultrasonic bubble dynamics data obtained in real-time in liquid metals in order to establish a reliable relationship between size-distribution and volume fraction of ultrasonic bubbles for different metal alloy melts. Such correlation is the basis for calculating the cavitation induced nucleation and the resulting effect of grain refinement.

In this paper, we developed a theoretical model to calculate and quantify the cavitation enhanced heterogeneous nucleation in an Al-Cu alloy melt under USMP. The model takes into account the acoustic intensity-dependent volume fraction and bubble size distribution obtained from synchrotron X-ray real-time imaging experiments. The relationship between the nucleus number and two important USMP parameters, i.e. input acoustic intensity and melt temperature was established. The results reveal that there exists a critical value for the input ultrasonic power (intensity) in order to achieve efficient grain structure refinement. The developed model and technical approaches can be exploited to other metal alloy systems.

2. Experiment

2.1. Ultrafast synchrotron X-ray imaging of ultrasonic bubble implosion and bubble population in Al-Cu alloys

The dynamic behavior of ultrasonic bubbles nucleation, oscillation and implosion in an Al-20 wt%t Cu alloy melt were studied at the sector 32-ID-B of the Advanced Photon Source (APS), Argonne National Laboratory using an imaging acquisition speed up to 271,554 fps. The experimental set-up and sample arrangement are shown in Fig. 1. A UP100H (from Hielscher) ultrasound generator and a Ti alloy sonotrode with a 2 mm diameter tip were used to generate and transmit the ultrasonic wave into the liquid metals when the melt temperature reached 700 ℃. The ultrasound input amplitude was set at 20% of the maximum amplitude (equivalent to an input ultrasound power density of ~44 W/cm^2 measured in water at the same amplitude) The frequency is 30 kHz. The X-ray parameters used, the operation procedure and subsequent image processing were described in detail in [12,13,16] and not repeated here.

Systematic in-situ imaging experiments were also conducted at the BL13W1 beamline of Shanghai synchrotron radiation facility (SSRF), China using an imaging acquisition speed of 3 fps. An Al-18wt.%Cu alloy was used.The equipment apparatus and parameters used were reported in [11]. The Al-18wt.%Cu melt temperature was maintained in the temperature range of 612 ~ 630℃ (the liquidus temperature was 611.3 °C measured by differential scanning calorimetry) during USMP. After that, the melt was cooled down to 610 ℃ in 1 min (a cooling rate of 0.03 ~ 0.33 ℃/s), and then decreased further to 550 ℃ in 10 min (a cooling rate of 0.1 ℃/s). The grain size of the solidification microstructure was measured and counted from the X-ray images. The recorded temperature profiles during and after USMP are showed in Fig. S1. The acoustic intensity applied was in the range of 0 to 150 MW/m^2 and the duration was 30 s. The nominal acoustic intensity is calculated by $\boldsymbol{I} = 1/2\rho c(2\pi f \boldsymbol{A})^2$ [8], where $\boldsymbol{A}$ is the vibration amplitude of the sonotrode tip, measured from the X-ray image.

The work at the SSRF was focused on studying the correlation between ultrasonic bubble size distribution, bubble volume fraction and the acoustic intensity as well as the resulting solidification microstructure in the Al-18wt.%Cu alloy. The obtained relationships were the essential data for the numerical model.

2.2. Synchrotron X-ray imaging and tomography studies of solidification microstructures

Synchrotron X-ray imaging and micro-tomography were used to study *in situ* the solidification microstructure . The micro-tomography experiments were conducted at the TOMCAT beamline of Swiss Light Source. An Al-15wt.%Cu was used in the in situ tomography work and details of the expeirments and data analyses were reported in [5], not repeated here again.. The X-ray radiography work relevant to the model validation (Section 4) was conducted at the beamline BL13W1 of SSRF using the same set up as the X-ray imaging of ultrasonic bubbles.

3. Model development and the relevant analytical equations

This section describes the analytical model for cavitation induced nucleation. Firstly, nucleation around a single bubble due to the pressure-spike induced undercooling is considered. Secondly, nucleation in a multi-bubble system generated by different levels of local acoustic intensity is addressed. Finally, nucleation in liquid melt under

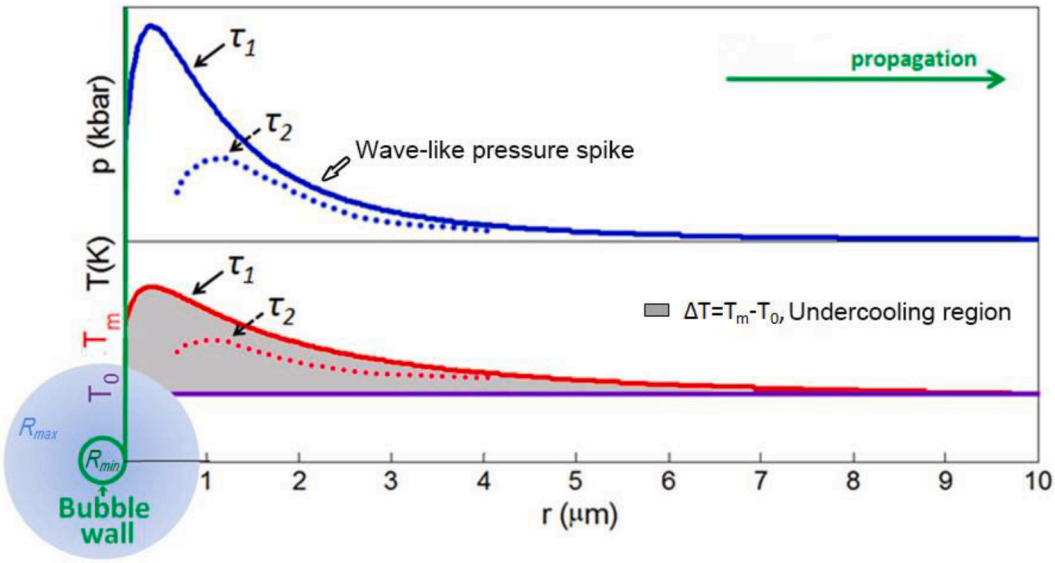

Fig. 2. A schematic, showing the temperature (red curves) and pressure (blue curves) profile nearby an imploding bubble. The bubble has two characteristic radii: R_{max} is the maximum radius of the bubble immediately before implosion, R_{min} is the minimum radius of the bubble immediately after implosion. The pressure induced undercooling (T_m-T_0) is indicated by the grey shaded region under the temperature profile.

USMP as function of input acoustic intensity and melt temperature is derived:

3.1. Nucleation due to a single cavitation bubble

Firstly, an ideal physical model is assumed, where only a single bubble is present in a liquid melt. The bubble is surrounded by an infinite melt with temperature variation across the bubble wall (see Fig. 2) [25]. At bubble implosion, the pressure is assumed to propagate outwards spherically [26] and any heat transfer from the imploding bubble to its surrounding melt is ignored (i.e. an adiabatic process) [22,24,27], The nucleation number at one-time implosion is calculated by

$$N_i = \int_{\tau}^{\cdot} \int_{V}^{\cdot} I_{nuc}(r,\tau) dV d\tau \tag{1}$$

where N_i is the number of nucleus, and the subscript i indicates the bubbles size; I_{nuc} is the nucleation rate in the undercooled volume V at time τ.

I_{nuc} is calculated by [28,29]:

$$I_{nuc} = I_0 \cdot exp\left(-\frac{\Delta G^*(T)\cdot f(\theta)}{kT}\right)\cdot exp\left(-\frac{Q}{kT}\right) \tag{2}$$

where k is the Boltzmann constant; $I_0 = nkT/h$; n is the atom number per unit volume, h is Plank constant; $\Delta G^*(T)$ is the energy barrier for the formation of a critical nucleus, given by:

$$\Delta G^*(T) = \frac{16\pi}{3}\cdot\frac{\sigma_{sl}^3 T_m^2 \cdot V_{mol}^2}{\Delta H^2 (T_m - T)^2} \tag{3}$$

where T_m is the melting temperature; ΔH is the enthalpy of phase change; V_{mol} is the molar volume of the solid phase; σ_{sl} is the solid–liquid interfacial energy. These parameters are normally constants at atmospheric pressure but considered as pressure-dependent in this research. In this work, the pressure dependent T_m is approximated by pure aluminum of the best Simon-fit [30],

$$T_m = T_{m0}\left(\frac{p}{60.49}+1\right)^{0.531} \tag{4}$$

where T_{m0} is a reference temperature. The undercooling at a specific location is calculated by

$$\Delta T = T_m(p) - T_0 \tag{5}$$

where T_0 is the local melt temperature. The phase change enthalpy ΔH in Eq. (3) is acquired by rewriting the Clausius-Clapeyron equation:

$$\frac{dlnT_m}{dp} = \frac{\Delta V}{\Delta H} \tag{6}$$

as

$$\Delta H = \Delta V \cdot \frac{dp}{dlnT_m} = \Delta V \cdot T_m \frac{dp}{dT_m} \tag{7}$$

where $\Delta V = V_s - V_l$ is the molar volume difference of solid (V_s) and liquid (V_l), considered constant. The $\frac{dp}{dT_m}$ is obtained by performing differentiation of the above melting-point expression. The interfacial energy σ_{sl} in Eq. (3) is obtained based on a deterministic function of the phase change enthalpy:

$$\frac{\sigma_{sl}}{\rho_s^{2/3}} = Cm^{1/3}\Delta H \tag{8}$$

where C is a constant and m is the atomic mass. The interface energy is simply obtained by comparing with a reference value:

$$\frac{\sigma_{sl}}{\sigma_{sl0}} = \left(\frac{\rho_s}{\rho_{s0}}\right)^{\frac{2}{3}}\cdot\frac{\Delta H}{\Delta H_0} \tag{9}$$

where ρ_s is the solid density; σ_{sl0}, ρ_{s0}, and ΔH_0 are the reference solid–liquid interface energy, the solid density, and the phase change enthalpy, respectively.

The Q in Eq. (2) is the activation energy for an atom diffusing across the liquid–solid interface, which is written as

$$Q = kTln\left(\frac{\eta V}{hN}\right) \tag{10}$$

where V is the molar volume of the liquid; N is the Avogadro constant; η is the absolute viscosity, which obeys the Arrhenius equation [31]:

$$\eta = \eta_0 exp\left(\frac{Q_a + p\Delta V_a}{RT}\right) \tag{11}$$

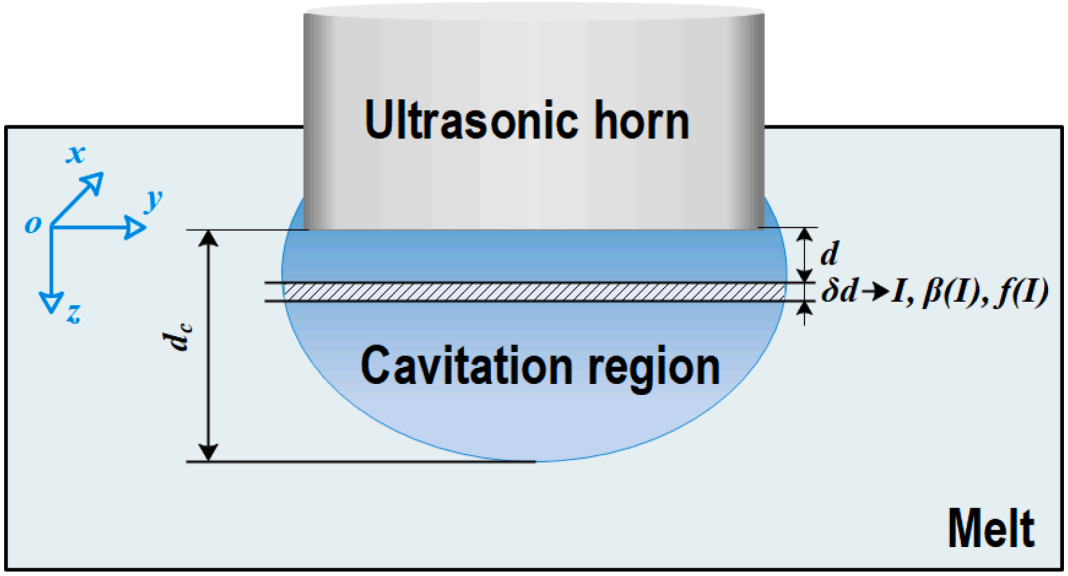

Fig. 3. A schematic, showing a typical cavitation zone, and how to link the local acoustic intensity I, bubble volume fraction $\beta(I)$ and size distribution $f(I)$, in the volume $d + \delta d$ in the cavitation zone. Note that the ultrasound irradiation face is set as zero in the z direction, and d_c indicates the cavitation depth [8].

where η_0 is a pre-potential viscosity factor; Q_a and ΔV_a are the activation energy and the activation volume, respectively. However, since the measured data for these parameters have not been seen reported for the Al-18 wt% Cu melt, The fitted data from pure aluminum melt in [32] were used in Eq. (11) for approximation. The explicit expression of η is

$$\eta = 0.29 \cdot exp\left(\frac{12000 + 1 \times 10^{-6} \cdot p}{8.31447 \cdot T}\right) \tag{12}$$

The $f(\theta)$ in Eq. (2) is the geometric factor, which is generally defined as [28]

$$f(\theta) = \frac{(1 - \cos(\theta))^2 \cdot (\cos(\theta) + 2)}{4}, \tag{13}$$

where θ is the wetting angle. The θ is influenced by many factors, such as substrate type and property, solid–liquid interfacial energy. Generally, the value is treated as a constant, independent of solute content as did in the work of [29,33,34]. In the present work, the wetting angle is simply considered as an angle between alumina and aluminum melt It is a relatively constant value of 86° at different temperatures for the polycrystalline aluminum with a surface roughness of 720 Å [35].

From Eqs. (1–12), I_{nuc} is a function of melt pressure p and the melt temperature T, and the nucleus number N_i in Eq. (1) is computed by finding p which is the pressure wave profile in the melt surrounding the imploding bubble.

To calculate the shock pressure, the characteristic method [36] based on the Kirkwood–Bethe hypothesis was used. According to the assumption, an invariant quantity $Y = r(h + u^2/2)$ propagates along outward "characteristic" curves with the characteristic velocity $c + u$, where r is the radial distance to the bubble center, and h, c, and u are the local enthalpy, velocity, and speed of sound in the liquid, respectively. The direction of the characteristic curves, as well as the velocity u and the pressure p_c along these curves, are given by [9]

$$\frac{du}{dt} = \frac{1}{r(c-u)}\left[(c+u)\frac{Y}{r} - 2c^2u\right] \tag{14}$$

$$\frac{dp_c}{dt} = \frac{n(p_c + B)}{rc(c-u)}\left[2cu^2 - \frac{c+u}{r}Y\right] \tag{15}$$

$$\frac{dr}{dt} = c + u \tag{16}$$

These equations are solved by integrating the velocity and pressure derivatives along the characteristic curves from the bubble wall as obtained from the Gilmore equation [9],

$$R\frac{dU}{dt}\left(1 - \frac{U}{C}\right) + \frac{3}{2}U^2\left(1 - \frac{U}{3C}\right) = H\left(1 + \frac{U}{C}\right) + \frac{RU}{C}\frac{dH}{dR}\left(1 - \frac{U}{C}\right), \tag{17}$$

where

$$C^2 = \frac{n(p_w + B)}{\rho_0}\left(\frac{p + B}{p_0 + B}\right)^{-1/n} \tag{18}$$

$$H = \frac{n}{n-1}\frac{(p_0 + B)^{1/n}}{\rho_0}\left[(p_w + B)^{n-1/n} - (p_\infty + B)^{n-1/n}\right] \tag{19}$$

$$p_w = \left(p_0 + \frac{2\sigma}{R_0}\right)\left(\frac{R_0}{R}\right)^{3\gamma} - \frac{2\sigma}{R} - \frac{4\mu U}{R} \tag{20}$$

where R and U denote the radius and velocity respectively; B and n are empirical constants which depend on the type of the liquid; σ , μ and γ are surface tension, the viscosity of the liquid and gas polytrophic exponent, respectively.

The diameter maxima (the maximum size of an oscillating bubble) was measured from the synchrotron X-ray images [8] and then set as the boundary condition to regress the Gilmore equation (17–20) to give the velocity and pressure derivatives for Eqs. (14–16).

3.2. Nucleation in a multi-bubble system

Theoretically, in a multi-bubble system the total nucleus number (N_I) is calculated by summating all bubble with size i in Eq. (11):

$$N_I = \sum_i n_i N_i \tag{21}$$

where n_i is the bubble number in group i. Mathematically, n_i is related to the bubble volume fraction β and the size-distribution $f(R_i)$ as

$$n_i = \beta \times \left(\int_{R_d}^{R_u} f(R) \cdot \frac{4}{3}\pi R^3 dR\right)^{-1} \times f(R_i) \tag{22}$$

where R_u and R_d are the upper and the lower limits of the integration, respectively. Here the bubble fraction and the size distribution of

cavitation bubbles vary in a whole ultrasonicated melt and dependent on the local acoustic intensity ($\beta(I)$ and $f(I)$ in δd region as schematically shown in Fig. 3. In this work, the data corresponding to the input acoustic intensity I_0 is first analyzed for the neighboring zone of ~ 1 mm beneath the radiation face based on the synchrotron radiation X-ray imaging results, and then the relations of ***I-β*** (acoustic intensity versus the volume fraction) and ***I-f*** (acoustic intensity versus the size distribution) can be regressed with varying I_0 in experiments. The detail can be found in our previous work [8]. Consequently, a hyperbolic tangent function was adopted to relate the bubble content $\boldsymbol{\beta}$ against the local intensity $\boldsymbol{I}$ [8,37] as

$$\boldsymbol{\beta} = \left(0.05\boldsymbol{tanh}\left(2\times10^{-4}\left(1.88\sqrt{\boldsymbol{I}}-11448\right)\right)+0.05\right) \tag{23}$$

The bubble size-distribution $\boldsymbol{f(R_i)}$ shows a log-normal distribution:

$$f(R_i) = \begin{cases} C_1 + \dfrac{C_2}{R_i\sigma\sqrt{2\pi}} e^{-\frac{\left[\ln\frac{R_i}{R_0}\right]^2}{2\sigma^2}}, R_1 < R_i < R_2 \\ 0, otherwise \end{cases} \tag{24}$$

where $\boldsymbol{R_1}$ and $\boldsymbol{R_2}$ are the minimum and the maximum size of recognizable cavitation bubbles in the synchrotron radiation X-ray images under a specific acoustic intensity; $\boldsymbol{\sigma}$ is the standard deviation; $\boldsymbol{C_1}$ and $\boldsymbol{C_2}$ are fitting constants. Readers are referred to Fig. S2, Fig. S3 and Table S1 for the fitting details. $\boldsymbol{f(R_i)}$ is functioned with $\boldsymbol{I}$ through the distribution parameters ($\boldsymbol{R_1, R_2, C_1, C_2, \sigma}$). For simplification, these parameters were linearly fitted to the acoustic intensity [8].

3.3. Nucleation in the liquid pool under USMP

Equations (21–24) calculate the nucleus density located in the region $\boldsymbol{[d, d+\delta d]}$ with the local acoustic intensity $\boldsymbol{I}$ in the $\boldsymbol{z}$-direction (normal to the ultrasound radiation face) as the schematic illustration in Fig. 3. For the whole melt, cavitation bubbles appear in a specific volume, namely the cavitation region (Fig. 3), and the nucleus would appear around the bubbles in this region according to the nucleation hypothesis. Due to attenuation, the local acoustic intensity $\boldsymbol{I}$ is not constant over the cavitation zone. Therefore, the total number of nuclei in the melt is an integration over the entire cavitation zone with different acoustic intensities.

With sound wave propagation in the melt, the local acoustic intensity can be expressed by:

$$\boldsymbol{I} = \boldsymbol{I_0}e^{-2\alpha(I)d} \tag{25}$$

where $\boldsymbol{\alpha(I)}$ is the I functioned local attenuation, and d is the distance from the radiation face.

In this work, the cavitation region $\boldsymbol{V_c}$ is approximated by the cavitation-depth [8] times the cross-section of the sonotorde radiation face [12]:

$$\boldsymbol{V_c} = \boldsymbol{s}\times\boldsymbol{d_c} \tag{26}$$

where $\boldsymbol{s}$ is the area of sonotrode radiation face, and $\boldsymbol{d_c}$ (Fig. 3) is the cavitation depth which is calculated by [8]

$$\boldsymbol{d_c} = -\frac{1}{2\boldsymbol{\alpha}(\boldsymbol{I_{th}})}\boldsymbol{ln}\left(\frac{\boldsymbol{I_{th}}}{\boldsymbol{I_0}}\right) \tag{27}$$

where $\boldsymbol{I_0}$ is the input acoustic intensity, and $\boldsymbol{I_{th}}$ is the cavitation threshold. Expression (27) is an implicit function of I and can be iteratively solved in combination with Eq. (25), as described in [8]. Finally, the total number of nuclei induced by cavitation ($\boldsymbol{N_{tot}}$) is written as

$$\boldsymbol{N_{tot}} = \int_{\boldsymbol{I_{th}}}^{\boldsymbol{I_0}} \boldsymbol{N_I}(\boldsymbol{I}) \int_0^{\boldsymbol{d_c}} (\boldsymbol{s}\bullet\boldsymbol{d})\boldsymbol{dzdI} \tag{28}$$

Equations (21–28) establish a relationship between the total number of cavitation induced nuclei in the whole melt ($\boldsymbol{N_{tot}}$) and the given ultrasonication parameters, input acoustic intensity($\boldsymbol{I_0}$) and melt temperature ($\boldsymbol{T_0}$), which can be numerically solved and with possible experimental validation. The computational procedure is as follows:

1) The simplified acoustic intensity field (z-direction gradient) and the cavitation depth are calculated based on Eqs. (25) and (27);
2) The acoustic intensity-dependent cavitation bubble volume and the size-distribution in each acoustic intensity equalized sub-volume are calculated by Eqs. (23–24);
3) The nucleus numbers in the sub-volumes described in step 2) are calculated by Eqs. (21–22) then;
4) The total nucleus number is finally acquired by accumulated the values from step 3) over each sub-volume according to Eq. (28).

The calculation parameters are listed in Table S2 in the supplementary material. The numerical process was programmed using MATLAB and computed using the high-performance computing (HPC) system at the National University of Singapore.

3.4. USMP enhanced structural refinement

Equation (28) predicts the total nucleus number from all the cavitation bubbles in the whole melt as a function of given input acoustic intensity and melt temperature. The assumption for such calculation is that each cavitation bubble only implodes once. To link the calculated nucleus number with the actual grain size measured from experiments, We used the well-known relationship between the number of active nuclei and the final grain size reported in [38], for USMP of an alloy with a duration (t), the final grain size ($\boldsymbol{D_{gs}}$) can be linked to the total nucleus number ($\boldsymbol{N_{tot}}$) by

$$D_{gs} = \left(\frac{0.5\bullet V_{pool}}{\int_0^t C_m\bullet f_u\bullet N_{tot}}\bullet dt\right)^{\frac{1}{3}} \tag{29}$$

where C_m is a correction factor and C_m is dependent on three factors: the oscillation-synchronicity of the cavitation bubbles, the stability of the nuclei in the melt, and then the nucleation efficiency of the nuclei. $\boldsymbol{f_u}$ is the cavitation frequency which can be considered as the same as the ultrasound frequency; and V_{pool} is the volume of the liquid pool under USMP. The underlying hypothesis of Eq. (29) is that the nuclei were homogeneously re-distributed in the melt owing to acoustic stream and each nucleus developed into one individual grain in the solidified alloy.

The oscillation synchronicity indicates the number of cavitation bubbles collapsing within the same oscillation period which contributes to the nuclei calculated in Eq. (28). A parameter a is introduced here to adjust the cavitation's non-synchronicity of which the cavitation bubbles appeared in one single synchrotron X-ray image and are employed as a group-cavitation-mode in the present model (cavitation induced nucleation is treated as an asynchronous event for different bubbles). In reality, the cavitation bubbles were experiencing the respective pulsating-moment/phase, however, they were recorded within the camera-exploring-time (preset 200 ~ 500 ms in the BL13W1 beamline) plus camera-response-time, and accumulated/overlapped in one X-ray image due to the relative low-time-resolution (the cavitation or pulsation period is around $T = 1/f_u = 50$ μs). The calibration is conducted as follows: (1) the ultrafast synchrotron X-ray imaging sequences (135780 fps) within the recording-time required (including the camera-exploring-time and the camera-response-time) for the low-time-resolution one (3 fps) were used to sampling; (2) the total number of cavitation events in a certain period (t_{sam}) and the number of bubble implosion captured in the same sequences were statistically analyzed as $\boldsymbol{N_{sam}}$ and $\boldsymbol{N_{imp}}$, respectively; (3) the value of a is then got as $a = \frac{N_{imp}}{N_{sam}}\bullet\frac{T}{t_{sam}}$, which values about 0.2 ~ 0.6 as the input acoustic intensity varies.

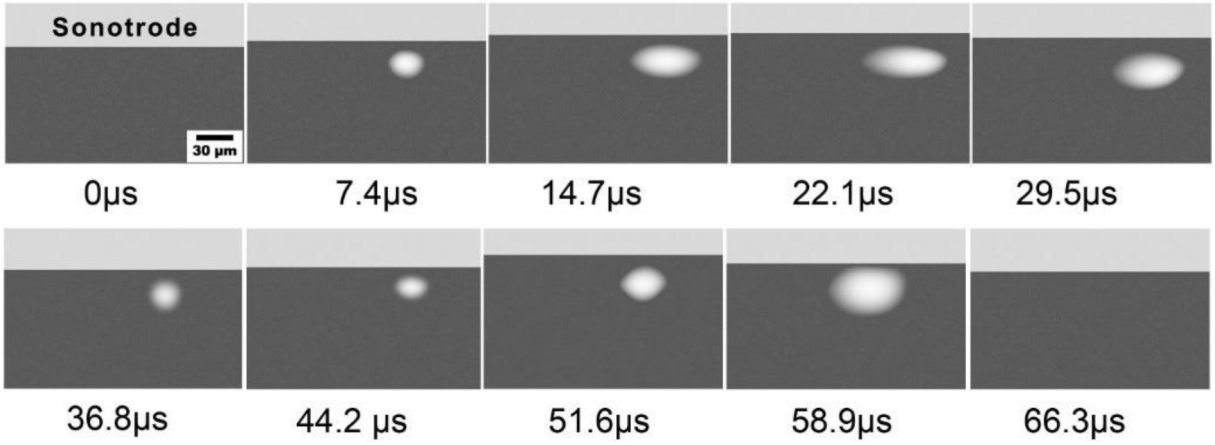

Fig. 4. Ultrafast synchrotron X-ray imaging of the nucleation, oscillation, and implosion of a single ultrasonic bubble in an Al-20 wt% Cu melt.

The nucleus stability concerns that the nuclei produced from former cavitation events would not keep a constant number in the melt during the subsequent USMP time due to re-melting etc., and the finally developed grains would not proportionally increase with the USMP time in the number. To count this, a new time-dependent parameter, η_t, is introduced to estimate the decay of the number of active nuclei within a specific USMP duration. Deducing from the evolution of the experimental grain size with treatment time [17,39], a well-fitted η_t as a function of varying USMP time (t) is obtained as follows (as shown in Fig. S4):

$$\eta_t = 0.77(t - 0.88)^{-0.12} \tag{30}$$

The nucleus nucleation-efficiency (f_g) indicates that only a small portion of the existing nuclei can successfully create new grains while the others lose the nucleation activity owing to the thermal diffusion or solute suppressed nucleation (SSN) effect [40] during the subsequent

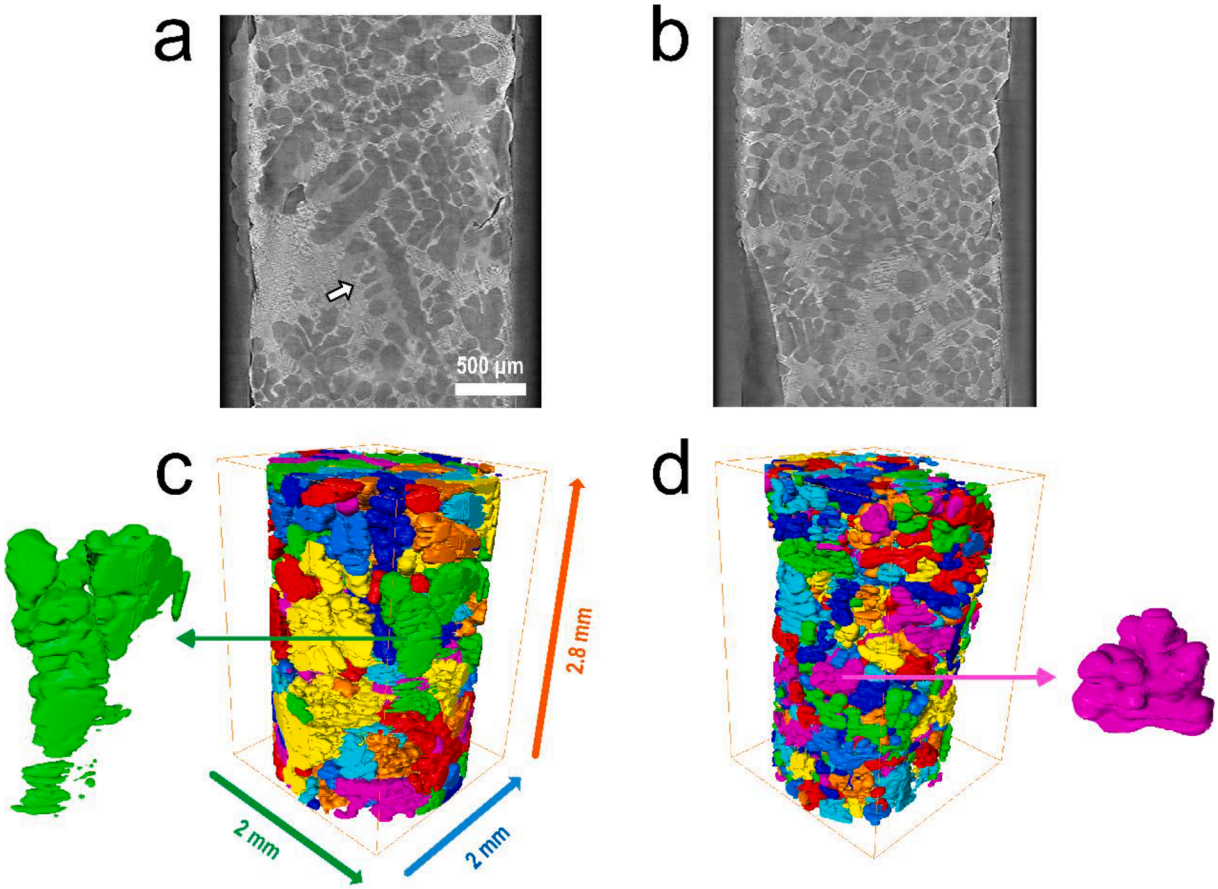

Fig. 5. Solidification microstructures of the Al-15wt.%Cu obtained by ultrafast synchrotron X-ray tomogrpahy[5](a, c) are without USMP; (b, d) are with USMP. (a, b) are the 2D projections of the 3D tomogrpahy datasets at the early stage of solidification with a low solid fraction (30 s after USMP with a cooling rate of 2 ℃/min). (c, d) are those at the later stage of solidification with a high solid fraction (the solidification is almost completed). Dendrites are shown in dark-grey in (a-b) and color segments in (c-d). The average equivalent diameter of the dendrites in (c-d) are~920 μm and ~290 μm, respectively. The predicted mean size of (d) is 228.6 μm calculated by the model with the input acoustic intensity of 5.8 MW/m^2, melt volume of 9.5 mm^3, at temperature of 630 ℃, and ultrasound processing time of 10 s.

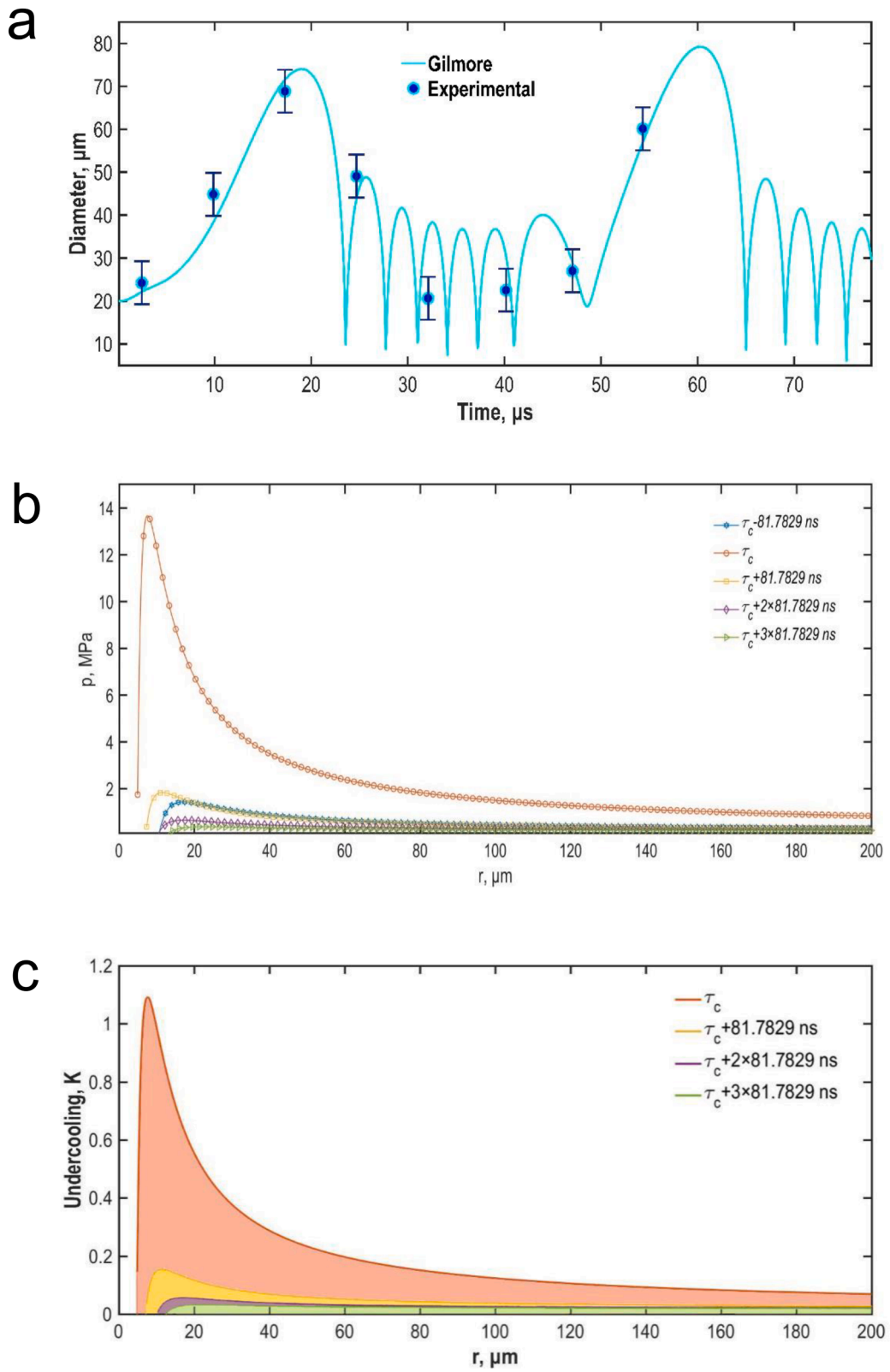

Fig. 6. (a) Bubble diameter evolution at implosion calculated by the Gilmore equation, (b) bubble implosion released pressure spike according to the characteristics method, and (3) the induced undercooling. The measured bubble diameters superimposed on Fig. 6a are those extracted from Fig. 4.. The pressure spike shown in Fig. 6b is from the first implosion at 23.5 μs (τ_c) exhibited in (a).

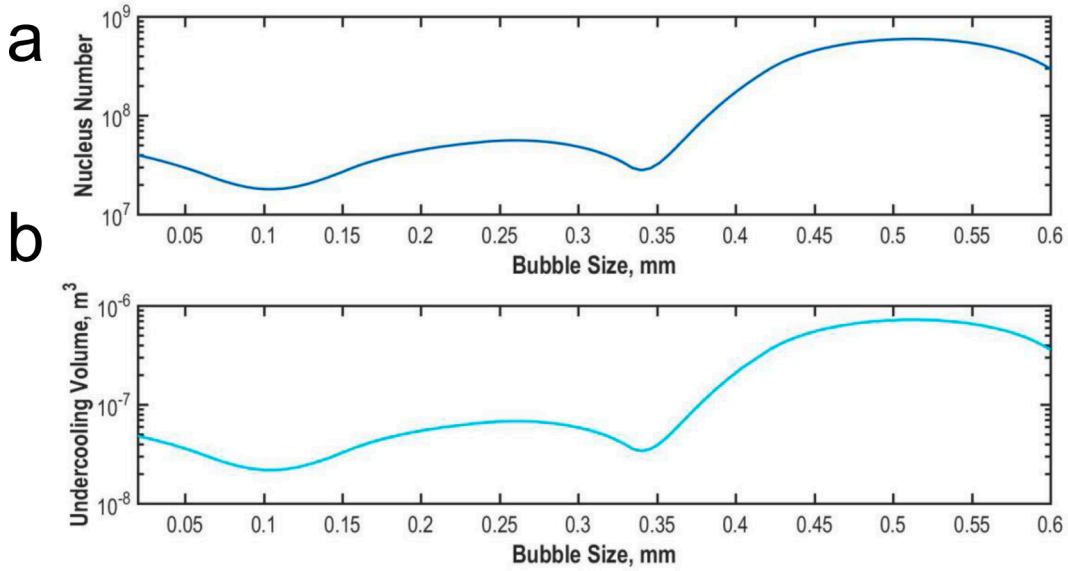

Fig. 7. (a) The calculated nucleus number,and (b) undercooling volume around a single cavitation bubble (as a funciton of the bubble size in radius).

cooling and solidification process. According to the previous quantitative work [40,41] based on the free growth model in refiner containing systems, the efficiency relies on their sizes and for the smaller nuclei, typically less than 1 μm for the cavitation induced nuclei [11], the efficiency is always around 5% irrespective of different cooling rates and refiner size-distributions [42]. With USMP, the efficiency is further increased [7], which is measured by a ratio ($\boldsymbol{n_m}$) to that without USMP ($\boldsymbol{f_{g0}}$), and the enhanced efficiency is got as

$$f_g = f_{g0} \bullet \mathrm{n_m}, \mathrm{f_g} < 1 \tag{31}$$

The values of $\boldsymbol{n_m}$ can be roughly assessed from experimental results with and without USMP for different refiner-alloy systems reported in literatures and are listed in Table S3 in the supplementary material, the data scatterred in a wide range of 0.24 ~ 17. To get rational $\boldsymbol{n_m}$ values for the present work, the probability-density distribution of the scattering data is analyzed as shown in Fig. S5. A range of 0.24 ~ 3 with higher probabilities (the accumulated probability near 80%) was adopted, while $\boldsymbol{f_{g0}}$ was fixed at 5% for simplicity.

Considering the above analysis of three aspects, an explicit C_m is given as

$$C_m = a \bullet \eta_t \bullet \mathrm{f_g} \tag{32}$$

which enables the calculation of Eq. (29) and the calculated results are compared with the experimental results.

4. Direct imaging of bubble implosion, oscillation and solidified grain structures

Fig. 4 shows the evolution of a single ultrasonic bubble captured by the ultrafast synchrotron X-ray imaging at 135,781 fps (a frame interval of 7.4 μs). The bubble was in a circular shape at 7.4 μs and expanded in subsequent frames (14.7 ~ 22.1 μs) as the sonotrode moved upwards (the rarefaction phase of the acoustic cycle) until to 22.1 μs. Then, the bubble imploded as the sonotrode moved downwards (29.5 ~ 36.8 μs, the compression phase of the acoustic cycle). The next frame at 44.2 μs shows that the bubble started the next cycle of expanding and then imploding. The real-time observation provided direct data and unambiguous evidence for validating the model in order to calculate the pressure spikes, i.e. the explosive waves around a imploding bubble. Notes that the cavitation bubbles exhibit nonspherical-shape more apparent in larger sizes (14.7 μs, 22.1 μs, 29.5 μs, 51.6 μs, and 58.9 μs) may due to larger pressure gradients..

Fig. 5 shows the 2D (Fig. 5a-b) and 3D (Fig. 5c-d) solidification microstructures of the Al-15wt.%Cu at different solid fractions. Coarse dendrites form in a large number without USMP (Fig. 5a) while fine and near equiaxed dendrites emerge with USMP (Fig. 5b) in the synchrotron X-ray images at their low solid fractions. Typically, dendrites in Fig. 5a exhibit long primary arms and well-developed second arms (arrow indicated) which, however, are unobvious in Fig. 5b. The micro-tomography rendered 3D morphologies in Fig. 5c-d differentiate their structures. Dendrites (partitioned in different colors) are in large sizes and effectively refined into smaller ones in the whole volume once USMP applied (around 920 μm reduced to 290 μm of the average equivalent diameter shown in Fig. 5c-d). Single grains extracted from Fig. 5c-d (sideways positioned and arrows indicated) elaborately show that the morphology of secondary dendrites degrades and the primary arms become ambiguous along with the size decrease. These intense contrasts give a direct evidence of the USMP caused structural refinement.

5. Model validation, discussion and application

5.1. Bubble implosion, pressure spike and the induced undercooling

Fig. 6a exhibits the Gilmore equation delineated the oscillation and the implosion of the single bubble (shown in Fig. 4), and compares with the experimental data (discrete points) measured from the ultrafast X-ray images. It is found that the Gilmore equation describes the cavitation behavior well. Fig. 6b plots the formation and propagation of the pressure spike at bubble implosion based on the characteristics method. The pressure spike formed at $\tau_c$exhibits a "pulse" shape and a high pressure-amplitude near the bubble wall (arrow denoted). The amplitude decreased exponentially (decreases almost 7 times within 81.7829 ns and less than 5 μm from the bubble wall) as the pressure spike propagated from the bubble wall. The amplitude attained tens of megapascals, resulting a large instantaneous undercooling around the bubble. Fig. 6c illustrates the time- and space-dependent undercooling around the imploded bubble according to Fig. 6b. The peak undercooling exceeds 1.1 K at the moment of implosion (i.e. minimum bubble size) and dropped to less than 0.2 K within 81.7829 ns, and the undercooling region (color-shaded) decreased as well. The undercooling is able to induce nucleation. It is noted that undercooling is influenced by the intensity of cavitation, which is again linked to the maximum bubble size..

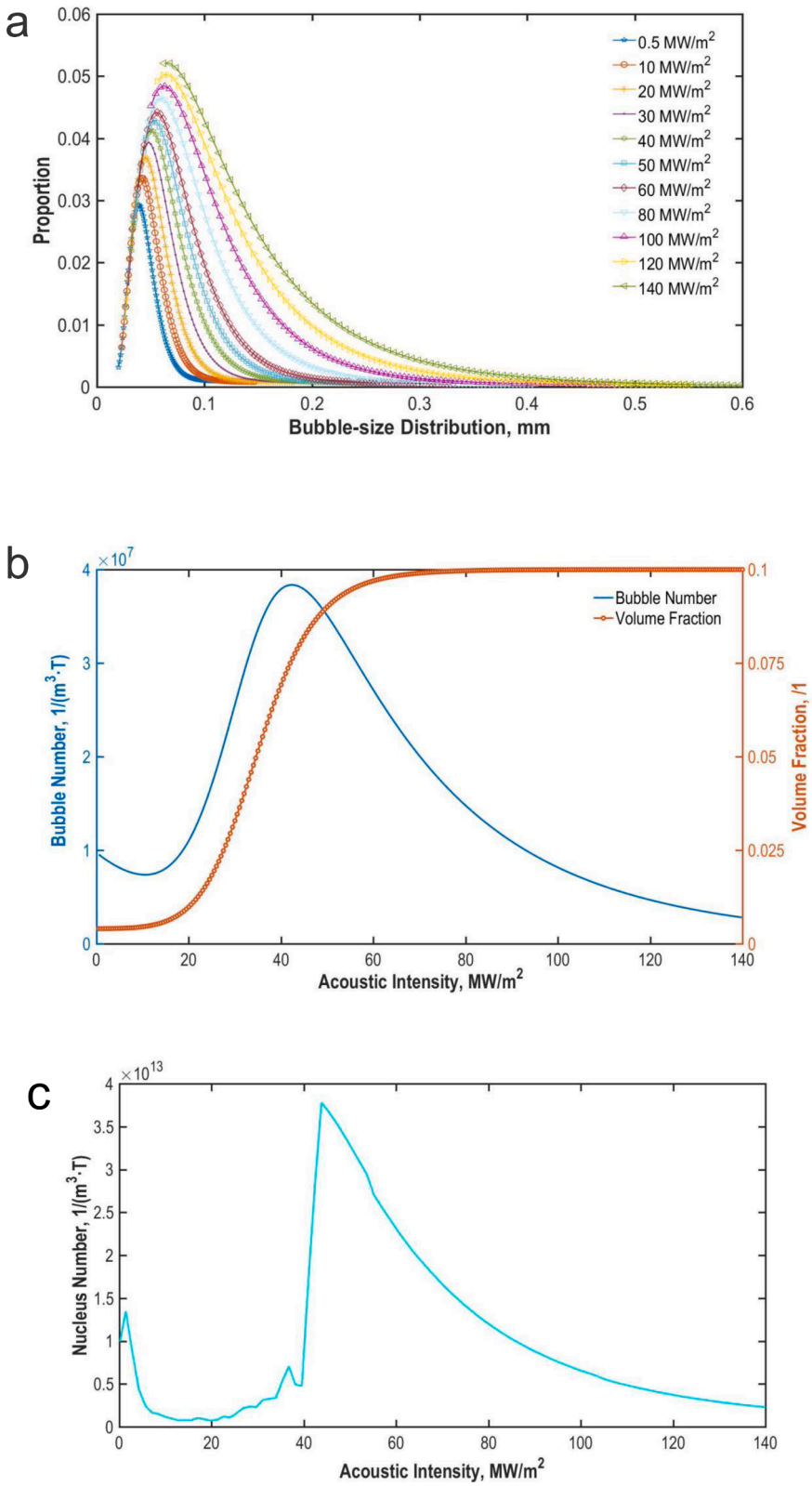

Fig. 8. (a) Size-distribution, (b) number density and volume fraction of cavitation bubbles, and (3) the nucleus number density from a multi-bubble system versus acoustic intensity in one period T of ultrasound waves.

5.2. Cavitation induced nucleation for a single bubble and multi-bubble system

Fig. 7 shows the calculated nucleus number induced by a single cavitation bubble with one-time implosion and the undercooling volume at a given acoustic intensity. The nucleus number tends to increase with the bubble size (measured from synchrotron X-ray images), although fluctuating at around 0.1 mm and 0.35 mm. The reason could be that the regression process of Gilmore equation induces numerical deviation and thus produces the fluctuation. The curve of undercooling volume against

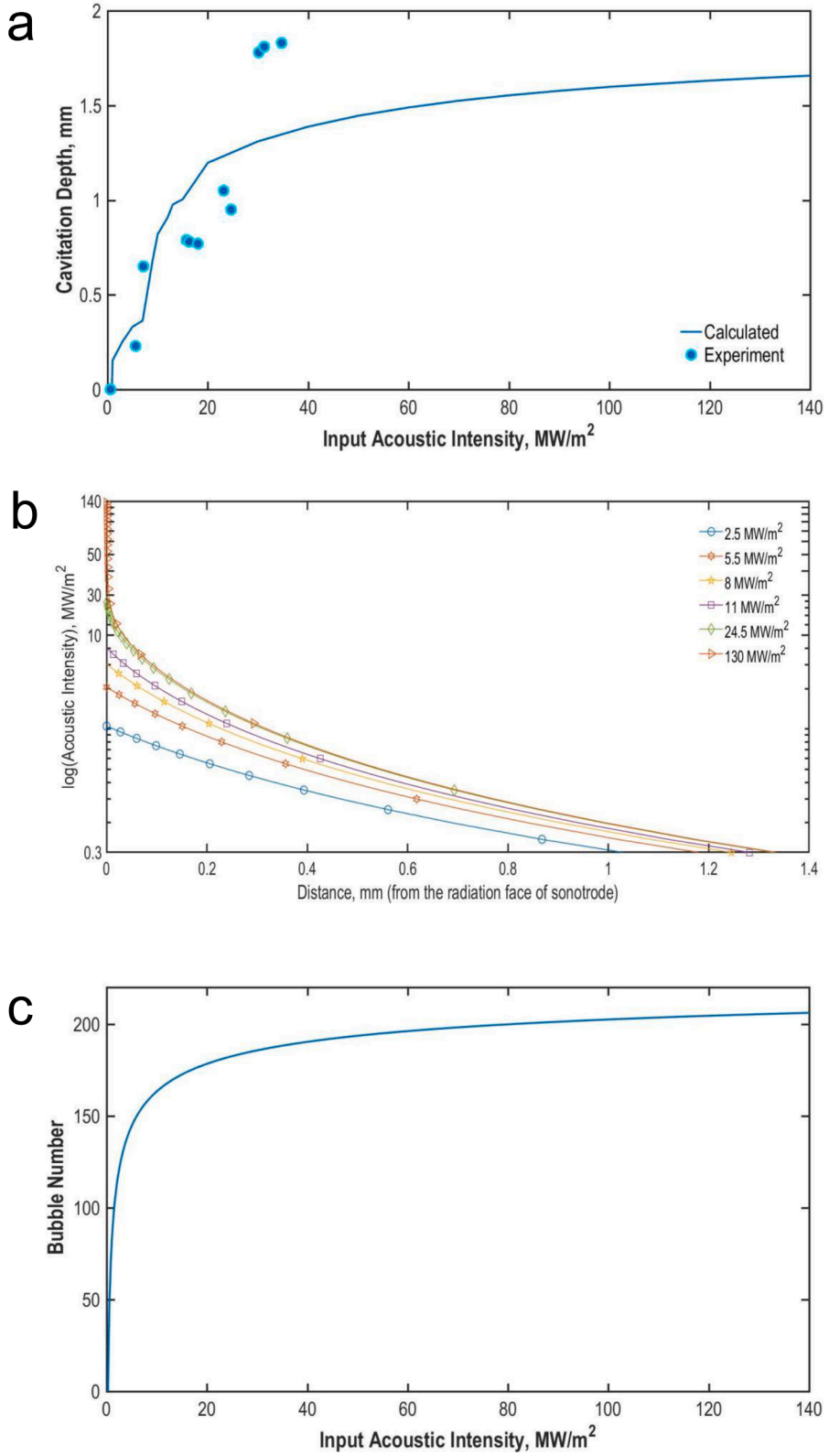

Fig. 9. (a) Variations of the cavitation depth, (b) the acoustic intensity gradient in the melt, and (c) the cavitation bubble number in a unit volume under USMP with different input acoustic intensities during one period *T* of ultrasound waves. The " 0 " position in the horizontal-axis in (b) indicates the ultrasound radiation face of the sonotrode.

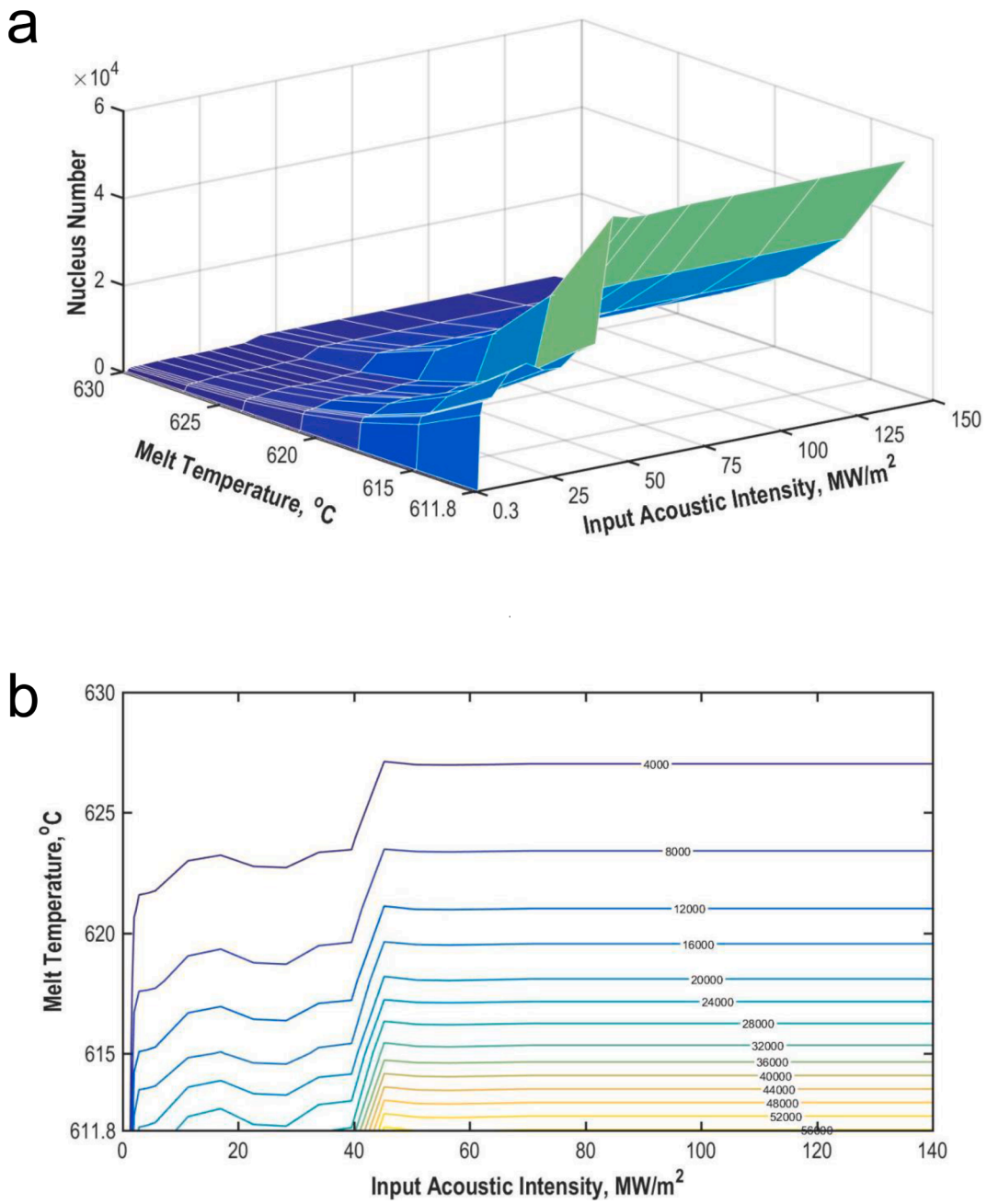

Fig. 10. (a) Nucleus number plotted with input acoustic intensity and melt temperature, and (b) the isopleth in the USMPed melt for one period T of ultrasound waves.

the bubble size almost exhibits the same trend, indicating that the nucleus number from a single bubble is dependent on the undercooling volume. A bigger bubble, generally, corresponds to more nucleus number for the larger undercooling volume.

Fig. 8 presents the bubble population and the nucleus number density in a multi-bubble system under different acoustic intensities for one period T of ultrasound waves. The size-distribution evolves according to Eq. (24) is exhibited in Fig. 8a. The mean value of the log-normal distribution, a size indication of most bubbles, monotonously increases with the acoustic intensity. Over the whole acoustic intensity range, the bubbles are almost less than 0.6 mm. Fig. 8b exhibits the volume fraction (given by Eq. (23)) and the corresponding bubble number density as the acoustic intensity increases. The bubble number density decreases initially due to the size increase and limited increase of the volume fraction until the acoustic intensity up to around 10 MW/m^2. The bubble number density then dramatically increases as the volume fraction rapidly enlarges, and gradually decreases when the volume fraction curve becomes flat. Fig. 8c presents the nucleus number per unit volume from a multi-bubble system calculated by Eq. (21), and the variation is roughly consistent with the bubble number density. The nucleus number diminishes when the acoustic intensity is in a range of 10 ~ 20 MW/m^2 and sharply increases up to the peak as the acoustic intensity is ~42 MW/m^2, then re-diminishes. The calculation shows that the bubble size and the bubble number density are two dominant factors to determine the nucleus number for a multi-bubble system and the bubble number density plays a leading role. More bubbles of larger sizes will produce much more nuclei in the melt.

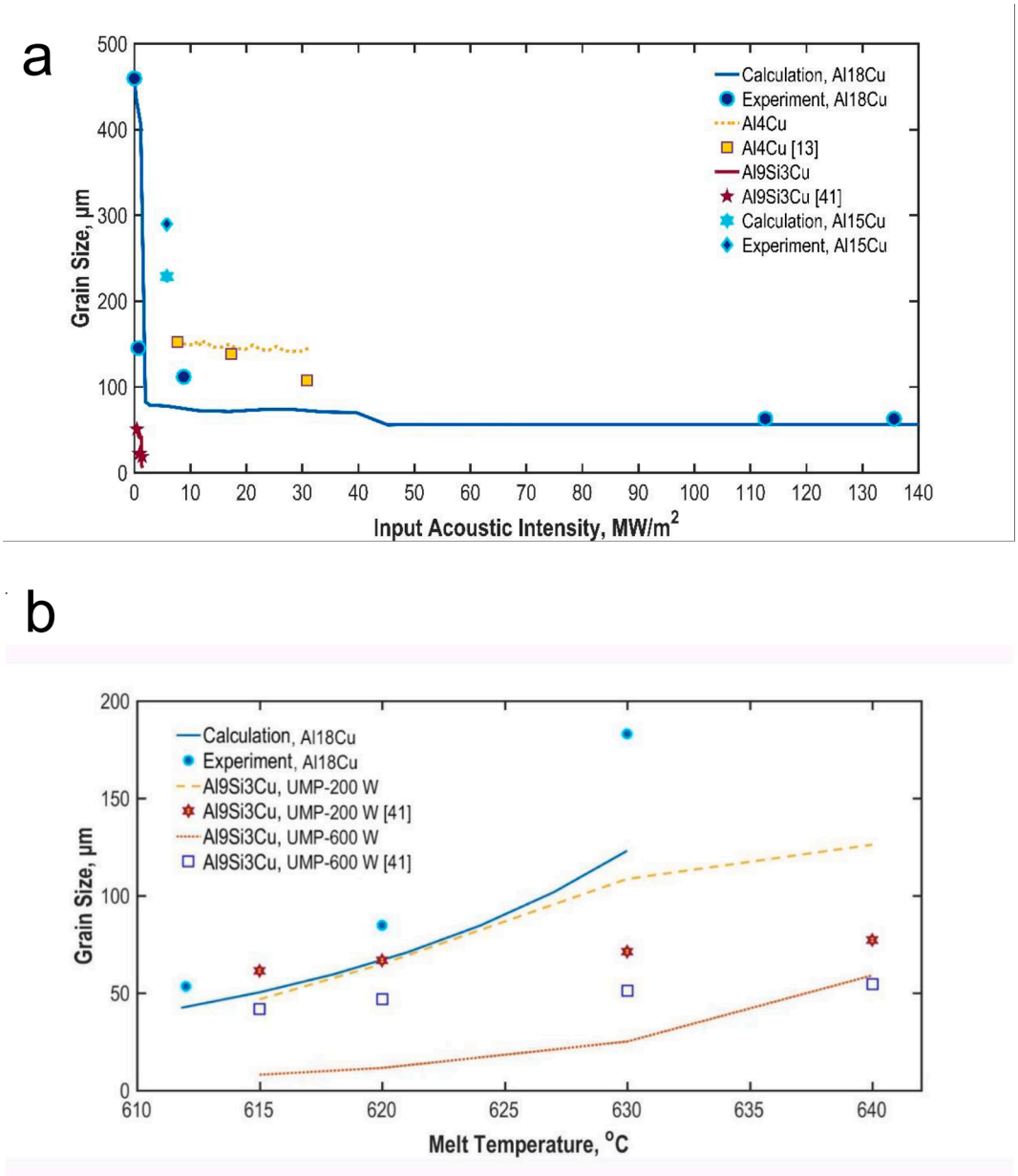

Fig. 11. (a) The calculated grain size versusacoustic intensity,and (b) melt temperature for different alloys with USMP. The experimental data of Al4Cu and Al9Si3Cu is from the reference [17] and [43], respectively.

5.3. *USMP enhanced nucleation in the melt*

Fig. 9a shows the calculated cavitation depth (a measure of the cavitation region in the present model) and comparison with the experimental data. Fig. 9b shows the calculated acoustic intensity gradient in the melt. Fig. 9c shows the total bubble number in the USMPed melt under different acoustic intensity inputs. The cavitation depth steadily increases with the input value in the range of 0 ~ 40 MW/m^2 (Fig. 9a). Generally, the increase of input acoustic intensity has two effects on the cavitation zone: increasing the volume fraction and size of cavitation bubbles (Fig. 8a-b) while giving rise to larger wave attenuation (indicated in Fig. 9b by the sharp decrease of acoustic intensity in the vicinity of the radiation face when the input is over 50 MW/m^2). An initial increase of the acoustic intensity input, typically below 20 MW/m^2 as exhibited in Fig. 8b causes the slow increase of the volume fraction and thus a minor attenuation to ultrasound propagation, which produced a quickly increased cavitation depth (Fig. 9a) and cavitation region [8]. In contrast, further enlarging the input intensity above 45 MW/m^2 leads to a rather slow increase in the cavitation depth. The calculated cavitation depth is well consistent with the experiment, except for a small deviation at higher acoustic intensity inputs where the experimentally observed cavitation depths were elongated by a severe drag-force from the acoustic stream [8]. This manifests that the cavitation depth and the cavitation region described in the present model are appropriate. Similar to the cavitation depth, the total bubble number shows a sharp increase when the input acoustic intensity is below 40 MW/m^2 and then to a moderate increase (Fig. 9c), due to a tradeoff between the increasing bubble volume fraction and increasing attenuation.

Fig. 10 shows the calculated nucleus number against the input acoustic intensity and the melt temperature in the USMPed melt for one period of ultrasound waves according to Eq. (28). An initial increase of the input acoustic intensity up to 20 MW/m^2 results in massive nucleation, although the bubble number density and the nucleus number density from a multi-bubble system decrease at each fixed acoustic intensity (Fig. 8b-c) in this range. The reason is that the dramatic

increment of the cavitation depth and the total bubble number in the USMPed melt (Fig. 9a-b) overcompensates the nucleus number reduction. The nucleation further accelerates with the input acoustic intensity increased and gives a boost in the range of 40 ~ 45 MW/m^2, attributing to a steep increase of the nucleus number density from a multi-bubble system (Fig. 8c), and the cavitation depth (Fig. 9). The attenuation to ultrasound extensively increases as to approach a plateau for the cavitation depth (Fig. 9a), owing to the significant increase in the bubble volume fraction. Over this range (greater than 45 MW/m^2), the bubble number in the USMPed melt slowly increases (Fig. 9c), but the size increment of the cavitation bubbles is maintaining the high increment of the nucleus number density (Fig. 8a and c, the size increment of cavitation bubble disproportionally matches that of the nucleus number density). As a result, the increment of the nucleus number becomes moderate along with the cavitation depth. Further increasing the input acoustic intensity produces a limited increase of the volume fraction to the plateau, and the total bubble number in the USMPed melt weakly increases (Fig. 9b). All of these responses by a negligible increase of the nucleus number. The influence of melt temperature on the nucleus number is more monotonous. The elevation of melt temperature causes the nucleus number steadily decreasing. Fig. 10b of an isopleth graph clearly shows the impact from the input acoustic intensity and the melt temperature.

Besides, Fig. 10 theoretically elucidates that increasing the ultrasound power to a specific value is enough to produce massive nucleation, such as an input acoustic intensity of 45 MW/m^2 in present work, and further increase of the power seems inefficient.

5.4. USMP induced microstructure refinement

To verify the model, a comparison between the calculated and the corresponding experiment was made, and the results are given in Fig. 11.

The grain size of Al-18wt.%Cu (Al-18Cu) in the present work decreases sharply with the input acoustic intensity above 5 MW/m^2 and further decreases until around 45 MW/m^2. Once exceeded the value, the input acoustic intensity becomes ineffective. The melt temperature increase monotonously coarsens the grains. These trends are well consistent with those of the nucleus number exhibited in Fig. 11, which unambiguously unveils that the cavitation induced nucleation is dominant to refine the solidified structure. The corresponding experimental data (points marked) are superimposed in Fig. 11, and aregenerally in line with the calculation except for an over-estimated around 10 WM/m^2. That originates from the solution of Gilmore equation which has a radius “jump” of the cavitation bubble, leading to a steep variation of the calculated nucleus number. The predicted Al-15wt.%Cu (Al-15Cu) shows a roughly comparable but smaller size than the experiment (the 3D solidification microstructures showed in Fig. 5), which may due to an overestimated nucleus number with a higher ultrasound frequency of 30 kHz, far larger than the experimental bubble statistics on a frequency of 20 kHz.

The current model is also validated by using other alloys as also exhibited in Fig. 11, assuming that the bubble population is the same as in Al-18Cu. The model calculations agree with the experiment in general when the acoustic intensity (for the cases of Al-4Cu and Al-9Si-3Cu) is used at the free variable.However, there are larger deviations when the melt temperature is used as the free variable..

6. Conclusions

An analytical model has been developed to predict the cavitation-enhanced undercooling and the solidification microstructures refined by ultrasonic melt processing (USMP). Ultrafast synchrotron X-ray imaging and tomography techniques were employed to collect the real-time experimental data for validating the model and the calculated results. The model takes into account of (1) the ultrasound input intensity, (2) cavitation bubble size and (3) melt temperature as the important parameters for predicting the cavitation induced undercooling and the solidified grain size. The results and comparison between modelling and experiments reveal that there exists an effective ultrasound input power density range for maximizing the grain refinement effect. Taking the Al-Cu alloy as examples, the ultrasound input intensity for effective grain refinement is in the range of 20 ~ 45 MW/m^2. In addition, a monotonous increase of the melt temperature has a negative effect on the number of nuclei under USMP and hence deteriorate the benefit on microstructure refinement due to the application of ultrasound.

CRediT authorship contribution statement

Haijun Huang: Conceptualization, Methodology, Investigation, Writing – original draft. **Ling Qin:** Methodology, Visualization, Writing – original draft. **Haibin Tang:** Software, Validation, Data curation. **Da Shu:** Formal analysis, Supervision, Funding acquisition. **Wentao Yan:** Supervision, Writing – review & editing, Funding acquisition. **Baode Sun:** Project administration. **Jiawei Mi:** Conceptualization, Writing – review & editing, Resources.

Declaration of Competing Interest

The authors declare that they have no known competing financial interests or personal relationships that could have appeared to influence the work reported in this paper.

Acknowledgments

Huang H., Shu D., and Sun B. would like to thank the financial support for this research by the National Natural Science Foundation of China (Nos. 51704196, U1832183, 51821001 and 51975393) and the Key R&D Program of Zhejiang Province (No.2021C01157).

Appendix A. Supplementary data

Supplementary data to this article can be found online at https://doi.org/10.1016/j.ultsonch.2021.105832.

References

[1] R.-G. Guan, D.i. Tie, A review on grain refinement of aluminum alloys: progresses, challenges and prospects, Acta Metall. Sin. 30 (5) (2017) 409–432.
[2] D.H. StJohn, M. Qian, M.A. Easton, P. Cao, Z. Hildebrand, Grain refinement of magnesium alloys, Metall. Mater. Trans. A 36 (2005) 1669–1679.
[3] X. Wang, Y.J. Hu, J.Y. Wang, W. Zhai, B. Wei, Microstructure evolution and mechanical property of quaternary Cu-7%Al-4%Ni-2.5%Mn alloy solidified within ultrasonic field, J. Alloys Compd., 881 (2021) 160604.
[4] D.G. Eskin, J. Mi, Solidification Processing of Metallic Alloys Under External Fields, Springer Series in Materials Science, ISBN: 978-3-319-94842-3 (2018) 1–320, https://doi.org/10.1007/978-3-319-94842-3.
[5] Z. Zhang, C. Wang, B. Koe, C.M. Schlepütz, S. Irvine, J. Mi, Synchrotron X-ray imaging and ultrafast tomography in situ study of the fragmentation and growth dynamics of dendritic microstructures in solidification under ultrasound, Acta Materialia 209 (2021), 116796, https://doi.org/10.1016/j.actamat.2021.116796.
[6] Y.J. Hu, X. Wang, J.Y. Wang, W. Zhai, B. Wei, Austenite Grain Refinement and Subsequent Martensite Transformation of Ternary Cu–Al–Ni Alloy Solidified Within Ultrasonic Field, Metall. Mater. Trans. A 52 (2021) 3097–3106.
[7] D.G. Eskin, I. Tzanakis, F. Wang, G.S.B. Lebon, T. Subroto, T. Pericleous, J. Mi, Fundamental studies of ultrasonic melt processing, Ultrasonics Sonochemistry 52 (2019) 455–467, https://doi.org/10.1016/j.ultsonch.2018.12.028.
[8] H. Huang, D. Shu, Y. Fu, G. Zhu, D. Wang, A. Dong, B. Sun, Prediction of Cavitation Depth in an Al-Cu Alloy Melt with Bubble Characteristics Based on Synchrotron X-ray Radiography, Metall. Mater. Trans. A 49 (2018) 2193–2201.
[9] D. Shu, B. Sun, J. Mi, P.S. Grant, A High-Speed Imaging and Modeling Study of Dendrite Fragmentation Caused by Ultrasonic Cavitation, Metall. Mater. Trans. A 43 (2012) 3755–3766.
[10] J. Hunt, K. Jackson, Nucleation of solid in an undercooled liquid by cavitation, J. Appl. Phys. 37 (1966) 254–257.
[11] H. Huang, D. Shu, J. Zeng, F. Bian, Y. Fu, J. Wang, B. Sun, In situ small angle X-ray scattering investigation of ultrasound induced nucleation in a metallic alloy melt, Scripta Mater. 106 (2015) 21–25.

[12] J. Mi, D. Tan, T.L. Lee, *In Situ* Synchrotron X-ray Study of Ultrasound Cavitation and Its Effect on Solidification Microstructures. Metallurgical and Materials Transactions B 46, Springer, 2015, pp. 1615–1619.
[13] D. Tan, T.L. Lee, J.C. Khong, T. Connolley, K. Fezzaa, J. Mi, High-speed synchrotron X-ray imaging studies of the ultrasound shockwave and enhanced flow during metal solidification processes, Metall. Mater. Trans. A 46 (2015) 2851–2861.
[14] H. Huang, D. Shu, Y. Fu, J. Wang, B. Sun, Synchrotron radiation X-ray imaging of cavitation bubbles in Al-Cu alloy melt, Ultrason. Sonochem. 21 (2014) 1275–1278.
[15] F. Wang, D. Eskin, J. Mi, C. Wang, B. Koe, A. King, C. Reinhard, T. Connolley, A synchrotron X-radiography study of the fragmentation and refinement of primary intermetallic particles in an Al-35Cu alloy induced by ultrasonic melt processing, Acta Mater. 141 (2017) 142–153.
[16] B. Wang, D. Tan, T.L. Lee, J.C. Khong, F. Wang, D. Eskin, T. Connolley, K. Fezzaa, J. Mi, Ultrafast synchrotron X-ray imaging studies of microstructure fragmentation in solidification under ultrasound, Acta Mater. 144 (2018) 505–515.
[17] S. Wang, J. Kang, Z. Guo, T.L. Lee, X. Zhang, Q. Wang, C. Deng, J. Mi, In situ high speed imaging study and modelling of the fatigue fragmentation of dendritic structures in ultrasonic fields, Acta Materialia 165 (2019) 388–397, https://doi.org/10.1016/j.actamat.2018.11.053.
[18] F. Wang, D. Eskin, J. Mi, T. Connolley, J. Lindsay, M. Mounib, A refining mechanism of primary Al3Ti intermetallic particles by ultrasonic treatment in the liquid state, Acta Mater. 116 (2016) 354–363.
[19] T. Inada, Z. Xu, A. Yabe, Active control of phase change from supercooled water to ice by ultrasonic vibration 1. Control of freezing temperature, Int. J. Heat Mass Tran. 44 (2001) 4523–4531.
[20] Z. Xu, T. Inada, A. Yabe, S. Lu, Y. Kozawa, Active control of phase change from supercooled water to ice by ultrasonic vibration 2. Generation of ice slurries and effect of bubble nuclei, Int. J. Heat Mass Tran. 44 (2001) 4533–4539.
[21] C. Virone, H. Kramer, G. Van Rosmalen, A. Stoop, T. Bakker, Primary nucleation induced by ultrasonic cavitation, J. Cryst. Growth 294 (2006) 9–15.
[22] M. Saclier, R. Peczalski, J. Andrieu, A theoretical model for ice primary nucleation induced by acoustic cavitation, Ultrason. Sonochem. 17 (2009) 98–105.
[23] C. Cogné, S. Labouret, R. Peczalski, O. Louisnard, F. Baillon, F. Espitalier, Theoretical model of ice nucleation induced by acoustic cavitation. Part 1: Pressure and temperature profiles around a single bubble, Ultrason. Sonochem. (2015) 447–454.
[24] F. Espitalier, R. Peczalski, S. Labouret, O. Louisnard, C. Baillon, Theoretical model of ice nucleation induced by inertial acoustic cavitation. Part 2: Number of ice nuclei generated by a single bubble, Ultrason. Sonochem. 28 (2016) 185–191.
[25] W. Kreider, L.A. Crum, M.R. Bailey, O.A. Sapozhnikov, A reduced-order, single-bubble cavitation model with applications to therapeutic ultrasound, J. Acoust. Soc. Am. 130 (2011) 3511.
[26] K. Johansen, J.H. Song, K. Johnston, P. Prentice, Deconvolution of acoustically detected bubble-collapse shock waves, Ultrasonics 73 (2017) 144–153.
[27] A. Prosperetti, Y. Hao, Modelling of Spherical Gas Bubble Oscillations and Sonoluminescence, Philos. T. R. Soc. B 357 (1999) 203–223.
[28] J. Valloton, S. Gawor, H. Henein, Modelling of nucleation in Impulse atomized undercooled droplets, Comp. Mater. Sci. 144 (2018) 176–180.
[29] Y. Xu, D. Zhao, Y. Li, A Thermodynamic Study on the Effect of Solute on the Nucleation Driving Force, Solid-Liquid Interfacial Energy, and Grain Refinement of Al Alloys, Metall. Mater. Trans. A 49 (2018) 1770–1781.
[30] R. Boehler, M. Ross, Melting curve of aluminum in a diamond cell to 0.8 Mbar: implications for iron, Earth Planet. Sci. Lett. 153 (3-4) (1997) 223–227.
[31] H. Terasaki, T. Kato, S. Urakawa, K.I. Funakoshi, A. Suzuki, T. Okada, M. Maeda, S. Jin, T. Kubo, S. Kasai, The effect of temperature, pressure, and sulfur content on viscosity of the Fe–FeS melt, Earth Planet. Sci. Lett. 190 (2001) 93–101.
[32] V.G. Postovalov, E.P. Romanov, V.P. Kondrat'ev, V.I. Kononenko, Theory of transport in liquid metals: calculation of dynamic viscosity, High Temp. 41 (6) (2003) 762–770.
[33] X. Yao, A. Dahle, C. Davidson, D. StJohn, Effect of solute on the growth rate and the constitutional undercooling ahead of the advancing interface during solidification of an alloy and the implications for nucleation, J. Mater. Res. 21 (2006) 2470–2479.
[34] X. Yao, A.K. Dahle, C.J. Davidson, D.H. StJohn, Modelling of grain size transition with alloy concentration in solidified Al–Si alloys, J. Mater. Sci. 42 (2007) 9756–9764.
[35] S. Ping, F. Hidetoshi, M. Taihei, N. Kiyoshi, Critical Factors Affecting the Wettability of α-Alumina by Molten Aluminum, J. Am. Ceram. Soc. 87 (2005) 1265–1273.
[36] V. Minsier, J. Proost, Shock wave emission upon spherical bubble collapse during cavitation-induced megasonic surface cleaning, Ultrason. Sonochem. 15 (2008) 598–604.
[37] C. Vanhille, C. Campos-Pozuelo, Acoustic cavitation mechanism: a nonlinear model, Ultrason. Sonochem. 19 (2) (2012) 217–220.
[38] Y. Xu, D. Casari, R.H. Mathiesen, Y. Li, Revealing the heterogeneous nucleation behavior of equiaxed grains of inoculated Al alloys during directional solidification, Acta Mater. 149 (2018) 312–325.
[39] Y.L. Li, H.K. Feng, F.R. Cao, Y.B. Chen, L.Y. Gong, Effect of high density ultrasonic on the microstructure and refining property of Al–5Ti–0.25C grain refiner alloy, Mat. Sci. Eng. A 487 (2008) 518–523.
[40] D. Shu, B. Sun, J. Mi, P. Grant, A quantitative study of solute diffusion field effects on heterogeneous nucleation and the grain size of alloys, Acta Mater. 59 (2011) 2135–2144.
[41] Q. Du, Y. Li, An extension of the Kampmann-Wagner numerical model towards as-cast grain size prediction of multicomponent aluminum alloys, Acta Mater. 71 (2014) 380–389.
[42] T.E. Quested, A.L. Greer, The effect of the size distribution of inoculant particles on as-cast grain size in aluminium alloys, Acta Mater. 52 (2004) 3859–3868.
[43] L. Zhang, D.G. Eskin, L. Katgerman, Influence of ultrasonic melt treatment on the formation of primary intermetallics and related grain refinement in aluminum alloys, J. Mater. Sci. 46 (2011) 5252–5259.
[44] M.H. Lu, Z. Wen, Q. Jiang, Nucleus–liquid interfacial energy of elements, Colloid. Surface A 278 (2006) 160–165.
[45] Y. Waseda, W.A. Miller, Calculation of the Crystal-Melt Interfacial Free Energy from Experimental Radial Distribution Function Data, Trans. Japan Inst. Met. 19 (1978) 546–552.